Anisotropic vortex channeling in $YBa_2Cu_3O_{7-\delta}$ thin films with ordered antidot arrays

A. Crisan,[1,2] A. Pross,[1] D. Cole,[1] S. J. Bending,[1] R. Wördenweber,[3] P. Lahl,[3] and E. H. Brandt[4]
[1]*Department of Physics, University of Bath, Claverton Down, Bath BA2 7AY, United Kingdom*
[2]*National Institute for Materials Physics, P.O. Box MG-7, Bucharest, 077125, Romania*
[3]*Institute of Thin Films and Interfaces (ISG2), CNI, Forschungszentrum Jülich D-52425 Jülich, Germany*
[4]*Max-Plank-Institut für Metallforshung, D-70506 Stuttgart, Germany*
(Received 21 November 2003; revised manuscript received 23 September 2004; published 14 April 2005)

Scanning Hall probe microscopy has been used to make a microscopic study of flux structures and dynamics in yttrium barium copper oxide thin-film disks containing a regular 10-μm-period square array of 2.5-μm-sized holes (antidots). Images obtained after field cooling the sample to 77 K in very low fields reveal that the holes can trap two flux quanta at this temperature. Scans obtained after zero-field cooling (ZFC) to 77 K and a subsequent applied field cycle clearly display preferential flux channeling along chains of antidots in the direction of maximum induction gradient. Remarkably, upon reversal of field sweep direction, we observe flux "streaming" out of the holes towards the sample edges with almost uniform density flux "stripes" bridging the holes in the exit direction. We estimate that the antidots can preferentially trap about 15 flux quanta in these ZFC experiments. Classical electrodynamics simulations of our samples appear to be in good qualitative agreement with our results, indicating that many of the observed phenomena may be geometrical effects that depend primarily on the shape and topology of the sample, and potential applications are discussed.

DOI: 10.1103/PhysRevB.71.144504 PACS number(s): 74.25.Qt, 74.25.Ha, 74.78.Bz, 74.78.Na

I. INTRODUCTION

Recently vortex ratchets, which exploit asymmetric vortex dynamics to achieve rectification and lensing effects, have been attracting considerable attention.[1] It has been shown both theoretically and experimentally that, in a superconductor with an asymmetric periodic potential achieved by having asymmetric channel walls, a graduated random pinning density, or periodic arrays of asymmetric pinning defects, an applied transverse ac electric current can lead to a net dc longitudinal transport of vortices.[2] It has recently been demonstrated that rectification of ac currents can take place in thin films containing asymmetric chains of large micron-sized antidots,[3] which is the motivation for the study reported here. The experimental realization of efficient vortex ratchets would enable a number of novel applications, including the removal of unwanted trapped flux in superconducting quantum interference devices (SQUIDs),[4] vortex pumps, and vortex lenses that can either disperse or concentrate vortices in chosen regions of a sample,[1] as well as collective vortex step motors.[5]

Furthermore, the optimization of conventional active and passive thin-film superconducting devices requires the suppression of dissipative processes due to the motion of vortices. In active devices vortex motion leads to increased low-frequency noise, reduced sensitivity, or increased bit error rate, while a reduction of quality factor and power handling capability results from their presence in passive microwave components. It is well known that vortex motion can be suppressed by sufficiently strong pinning centers in the superconductor, which can be created by high-energy neutron or heavy-ion irradiation,[6] by randomly distributed self-assembled nanodots grown on the substrate before film deposition,[7] or by the fabrication of a regular array of (sub)micron artificial defects (holes or magnetic dots).[8] In $YBa_2Cu_3O_{7-\delta}$ (YBCO) SQUIDs, a few strategically positioned antidots have been shown to trap vortices and, hence, to reduce the noise.[9]

Most experimental studies of vortex ratchets have been based on systems of nanoscale pinning sites that are typically only capable of pinning ~ 1 superconducting vortex. Recently, however, an unexpected fourfold symmetry of flux penetration was observed in magneto-optical measurements on a circular YBCO thin-film disk containing a square array of very large (~ 2-μm-diam) antidots. This observation was quantitatively explained using a simple vortex channeling model where the angle between the normal to the sample edge and the closest unit vector of the antidot lattice is the most important parameter.[10] The high-resolution studies reported here complement this magneto-optical imaging work with a view to understanding the vortex dynamics in very similar samples at the microscopic level. While our measurements confirm the picture of Ref. 10, we also demonstrate that the presence of antidots in these films can induce an intrinsic asymmetry in the dynamics of flux penetration and exit, making this an especially promising system for the fabrication of ratchet devices. Many of the phenomena that we observe appear to be qualitatively reproduced in classical electrodynamics simulations of "model" samples, which suggests that they may arise from geometrical effects that depend primarily on the shape and topology of the sample, and flux quantization seems to play a secondary role.

The most direct information regarding vortex structures and dynamics is obtained through local measurements of the magnetic field within or at the surface of a superconducting sample. In this investigation we have made extensive use of high-resolution scanning Hall probe microscopy (SHPM) to investigate flux dynamics (penetration and exit, channeling, and local magnetization) in two patterned YBCO thin films (a 2 mm $\times$ 2 mm square and a 2-mm-diam disk) containing a regular square array of micron-sized holes (antidots). SHPM images were acquired under various conditions, with samples field cooled (FC) or zero-field cooled (ZFC) and subjected to different applied field histories. The results are discussed in the context of existing theoretical models and

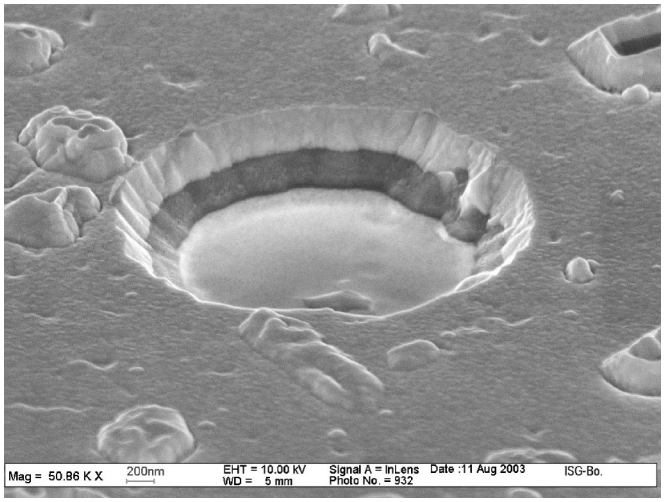

FIG. 1. Scanning electron micrograph image of a typical antidot.

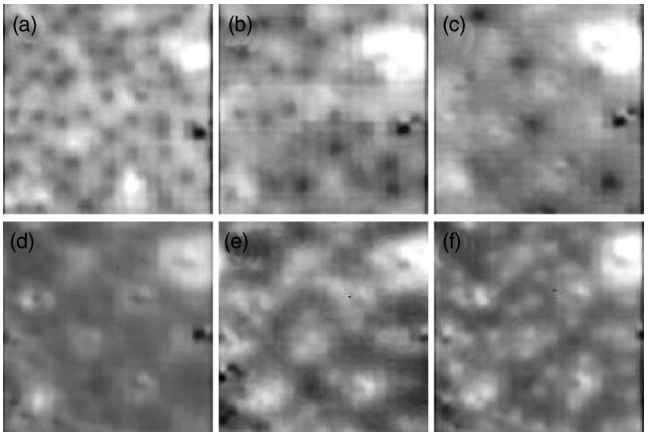

FIG. 2. SHPM scans on the YBCO disk after field cooling to 77 K in (a) −1.6 Oe [grayscale spans (GS) ~1.4 G], (b) −1.1 Oe (GS~1.7 G), (c) −0.6 Oe (GS~1.9 G), (d) 0.4 Oe (GS ~2.8 G), (e) 0.7 Oe (GS~3.6 G), and (f) 0.9 Oe (GS~2.1 G).

practical applications of antidots in cryoelectronic devices described.

II. EXPERIMENT

In order to create a superconductor with tailored flux pinning properties that can be examined with SHPM, optical lithography and ion beam etching were used to pattern antidots in a magnetron sputtered $YBa_2Cu_3O_{7-\delta}$ film grown epitaxially on a CeO_2-buffered sapphire substrate. A scanning electron micrograph (SEM) of a typical antidot is shown in Fig. 1. Two samples have been investigated that both consist of a 200-nm YBCO thin film containing 2.5-μm-diam antidots on a square 10-μm period lattice. One sample had been patterned into a 2 mm$\times$2 mm square (with the antidot lattice vectors parallel to the edges) and a second into a 2 -mm-diam disk. In both cases T_c=88 K.

A state-of-the-art scanning Hall probe microscope has been used in this study. The Hall sensor was patterned in a GaAs/AlGaAs heterostructure two-dimensional electron gas and consists of a 0.8-μm resolution Hall probe and an integrated scanning tunneling microscope (STM) tip formed by coating the corner of an etched mesa with a thin layer of gold. This probe was bonded onto the end of the piezoelectric scanner tube of a commercial low-temperature scanning tunneling microscope (STM). The YBCO film was stuck onto a separate sample puck, which was tilted 1°–2° with respect to the Hall probe to ensure that the STM tip (situated at the corner of the chip, about 13 μm away from the Hall probe) was always the closest point to it, and brought into tunnelling contact with a "stick-slip" inertial approach mechanism. Our SHPM is described in more detail elsewhere.[11] The microscope was placed in a cryostat containing a 65–300 K variable-temperature insert and an external copper coil capable of generating magnetic fields, H, up to ~32 Oe perpendicular to the sample. The experiments were performed in a "flying" mode whereby the STM tip is used to find and map the surface after which the sample is retracted a fixed distance ($\geqslant$0.5 μm) out of tunneling contact in order to perform rapid magnetic imaging without STM feedback. In the measurements presented here, the scan area is about 32 μm$\times$32 μm, and divided into 128$\times$128 pixels. Each pixel has been averaged 13 times and the presented images typically correspond to the average of 25–100 consecutive full scans in order to suppress low-frequency $1/f$ noise. This procedure results in a two-dimensional map of the local magnetic induction, B_{ij} $(i,j=1-128)$, as well as an average value of induction over the entire scan area and a grayscale (GS), $\delta B=\mathrm{Max}(B_{ij})$-$\mathrm{Min}(B_{ij})$. All data presented in this paper were captured at 77 K at about 0.5 mm from the edge in the case of disk-shaped sample, and about 0.3 mm from the closest edge for the square sample. Under these circumstances we observe qualitatively the same phenomena in both the square and disk-shaped samples.

III. RESULTS

A. Field-cooled SHPM scans

Figure 2 illustrates typical images of flux structures in the disk-shaped sample after field cooling from 90 to 77 K in a range of very small fields: (a) −1.6 Oe, (b) −1.1 Oe, (c) −0.6 Oe, (d) 0.4 Oe, (e) 0.7 Oe, and (f) 0.9 Oe. The quality of these (and subsequent) images is not optimal due to the surface roughness of the patterned films (see Fig. 1), which prevents us from getting close to the YBCO surface where peak vortex fields are much higher. Surface roughness also gives rise to image artifacts due to electrostatic coupling ("gating") between the Hall probe and the sample at topographic peaks (e.g., the intense quadrupolelike feature at the right-hand edge of all images in Fig. 2). Since the sample is roughest in the vicinity of the antidots, this does, however, make their locations readily identifiable [e.g., the square array of bright circles in Fig. 2(d)] and allows the induction profiles to be correlated with their positions. This electrostatic contrast at the antidots tends to dominate over the magnetic contrast due to flux residing there (at low fields), making it difficult to directly estimate the number of trapped vortices. Fortunately this number can be inferred indirectly

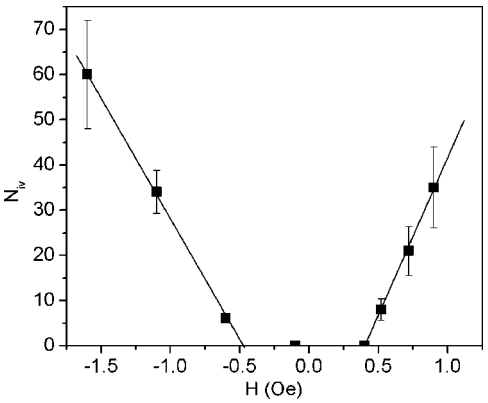

FIG. 3. Number of interstitial vortices vs applied cooling field for images on the YBCO disk at 77 K. The lines are a guide to the eye.

by counting the number of *interstitial* Abrikosov vortices, which can be clearly observed as dark dots for negative fields [Figs. 2(a)–2(c)] or white dots for positive fields [Figs. 2(e) and 2(f)]. The apparent vortex diameter [full width at half maximum (FWHM) $\sim$3.5 μm] is controlled by the size and lift-off of the Hall sensor under these circumstances, and is significantly larger than twice the expected penetration depth at this temperature. In Fig. 2(d) ($H=0.4$ Oe), we observe no interstitial vortices and conclude that all flux is trapped within the antidots. The effective saturation trapping number (n_s) for an antidot can be estimated by counting the number N_{iv} of interstitial vortices in images at various fields (Fig. 3). Extrapolating these data to $N_{iv}=0$ we see that no interstitial vortices form in the range -0.4 Oe$\leqslant H \leqslant 0.4$ Oe, when all the flux is trapped in the holes. Using the definition of magnetic induction $B=n_s\phi_0/D^2$, where $D=10$ μm is the antidot lattice periodicity, we infer a saturation trapping number of $n_s \approx 2$ at 77 K.

Figure 4 illustrates the situation in the disk-shaped sample at 77 K as the applied field is gradually reduced to zero from the field-cooled value of 24 Oe. Figure 4(a) is an image immediately after field cooling and the very weak contrast shows that the mean flux line density in the antidots and interstitial film is almost the same at these fields. As the applied field is reduced from 24 Oe the images (not shown) remain the same as Fig. 4(a) until $H \leqslant 20$ Oe. A further decrease in field to 20 Oe [Fig. 4(b)], 16 Oe [Fig. 4(c)], and 0 Oe [Fig. 4(d)] leads to a progressive increase in image contrast. By analyzing a sequence of many magnetic induction images as the field is gradually removed, we conclude that this arises due to flux in the antidots readily flowing out of the sample while the interstitial flux remains largely

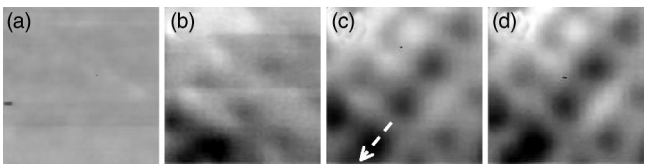

FIG. 4. SHPM scans on the YBCO disk after field cooling to 77 K in 24 Oe (a) (GS$\sim$0.8 G) and subsequently reducing the field to (b) 20 Oe (GS$\sim$1.6 G), (c) 16 Oe (GS$\sim$2.2 G), and (d) 0 Oe (GS$\sim$2.5 G).

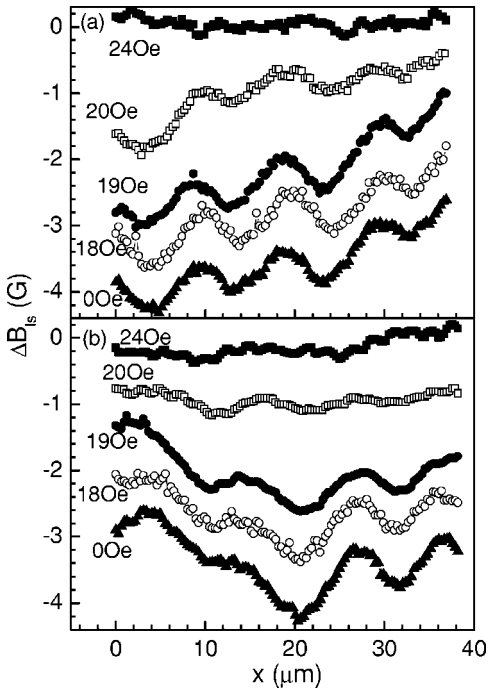

FIG. 5. Line scans (vertically offset for clarity) across chains of antidots at various applied fields for a YBCO disk after field cooling to 77 K in 24 Oe. (a) Along the lattice vector towards the closest point on the edge of the sample. (b) Perpendicular to line (a) [see arrows in Fig. 4(c)].

pinned and immobile. In this way the emptying antidots obtain a black contrast ($B_{local}\sim 0$) in the image at $H=0$ Oe because all the remanent (white) flux is sited interstitially. We note that the flux leaving the holes appears to be channeled towards the film edge along one of the unit vectors of the antidot lattice in which the magnetic induction gradient is maximum. To confirm this interpretation, Fig. 5 shows a sequence of line scans (vertically offset for clarity) along the directions indicated in Fig. 4(c) either towards the nearest edge of the sample [Fig. 5(a)] or perpendicular to it [Fig. 5(b)]. As expected, the maximum induction gradient builds along the direction towards the nearest edge of the sample once the applied field is reduced below 20 Oe. Perpendicular to this we see that, while the degree of channeling is quite inhomogeneous for adjacent antidot chains, very little overall induction gradient forms as the field is removed. This appears to be a microscopic confirmation of the phenomenon leading to the fourfold symmetry recently reported during flux penetration in similar samples in Ref. 10. This indicates a strong interaction between supercurrents circulating the holes and those due to bulk induction gradients, similar to that revealed in magneto-optical images of flux penetration in a YBCO film with several larger (40-μm) circular holes.[12] While we believe that the vortices flow out of the sample upon field removal, we cannot rule out the possibility that antivortices are channeling in the opposite direction, and the process is one of systematic vortex-antivortex annihilation. The latter would be the expected mechanism of magnetization reversal in homogeneous thin films.[13]

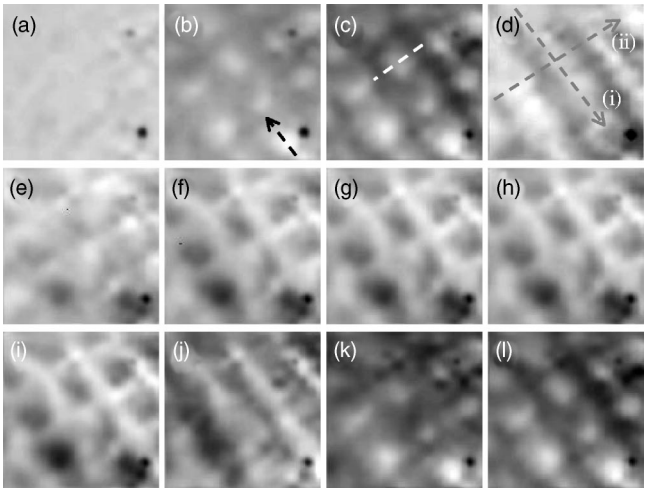

FIG. 6. SHPM scans on the YBCO square after ZFC to 77 K followed by an applied field sweep between 0 and ±32 Oe: (a) H =1 Oe (GS ~ 1.4 G), (b) 4 Oe (GS ~ 4.4 G), (c) 32 Oe (GS ~ 4.7 G), (d) 28 Oe (GS ~ 2.9 G), (e) 24 Oe (GS ~ 4.6 G), (f) 12 Oe (GS ~ 4.7 G), (g) 0 Oe (GS ~ 4.9 G), (h) −16 Oe (GS ~ 5.0 G), (i) −32 Oe (GS ~ 5.0 G), (j) −28 Oe (GS ~ 2.8 G), (k) −24 Oe (GS ~ 4.6 G), and (l) 0 Oe (GS ~ 5.0 G). Lines (i) and (ii) in (d) indicate the directions of the line scans shown in Fig. 8.

B. Zero-field-cooled SHPM scans

Figure 6 shows typical images of the ZFC square YBCO sample (T=77 K) at various points on a subsequent applied field cycle (increasing to 32 Oe, decreasing to −32 Oe and increasing again to zero). Once again two intense topographic image artifacts are visible at the right-hand edge of all scans, and the grayscale (GS) quoted in the figure caption has been estimated after cropping these out. As H is increased from zero to 1 Oe, all the scans look similar to Fig. 6(a), having a very low GS and no obvious features that can be attributed to the square array of antidots. At 4 Oe [Fig. 6(b)] flux has begun to penetrate this area of the sample, residing predominantly in the holes. Again a careful analysis of sequential images appears to show that vortices are channeled into the sample along the antidots in the direction of the maximum induction gradient [arrow in Fig. 6(b)], and the periodic white spots in the image now reflect the positions of the antidots. Evidently the penetration field measured in this way will depend on the location of the scan area within the sample. Although many more vortices enter the sample as the field is increased to the maximum value of H_0=32 Oe [Fig. 6(c)], the images all look very similar, apart from a slight increase in grayscale. This indicates that the flux line density in the holes is higher than in the surrounding interstitial film, and this difference only depends weakly on the applied field (H>4 Oe). Due to the very strong overlap of the induction profiles associated with neighboring antidots, it is not possible to use the image grayscale to estimate the amount of additional trapped flux directly. Instead a phenomenological three-parameter model has been used to fit the data at high fields, allowing an estimation of the actual number of flux quanta trapped in each antidot. Assuming that the image contrast arises due to supercurrents circulating around the holes that decay exponentially in the radial direction with

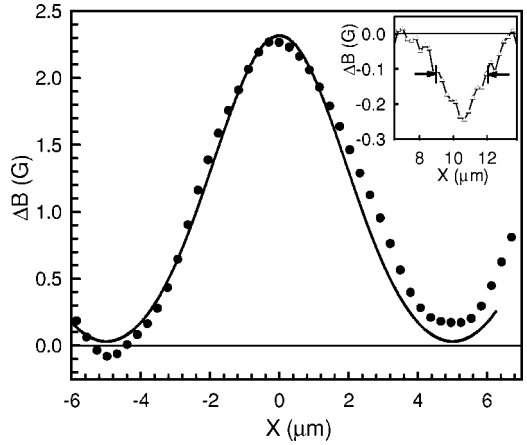

FIG. 7. Fit of phenomenological model (see text) to flux profile measured along the line indicated in Fig. 6(c). The inset shows a line scan across one of the black Abrikosov vortices shown in Fig. 2(b).

a characteristic penetration depth, λ_{eff}, the field measured at a height, z_0, and a radial distance, r_0, from the center of an antidot in the YBCO film is given by

$$B_z(r_0,z_0) = \mu_0 H_a - \frac{\mu_0}{4\pi}\int_{-d/2}^{d/2}\int_{R}^{\infty}\int_{0}^{2\pi} \times \frac{J_c \exp[-(r-R)/\lambda_{\mathrm{eff}}]r(r-r_0\cos\theta)d\theta dr dz}{[r_0^2+r^2-2rr_0\cos\theta+(z_0-z)^2]^{3/2}}, \quad (1)$$

where R is the antidot radius, d is the thickness of the film, and J_c is a characteristic critical current density. The actual scanning height used in the experiments has been estimated from line scans [see inset of Fig. 7] of the black Abrikosov vortices shown in Fig. 2(b). The full width at half maximum obtained from this analysis is ~3.5±0.5 μm, very much larger than either the expected vortex diameter or the dimensions of the Hall probe used. The only other source of broadening is that due to the flying height of the Hall probe above the sample, allowing us to identify z_0 in Eq. (1). Assuming a homogeneous filling of the antidots at high fields, Eq. (1) has been summed over an infinite antidot lattice in Fourier space, and then fitted to typical ZFC flux profiles with λ_{eff} and J_c as free parameters. Figure 7 shows the line scan captured in the direction shown in Fig. 6(c) along with a fit to the model for λ_{eff}=0.65 μm and $J_c=6\times10^6$ A/cm^2. This value for the effective penetration depth is reasonable, being slightly smaller than the Pearl length[14] for very thin films $\Lambda=\lambda(T)^2/d=(0.37)^2/0.2=0.68$ μm. The fitted value of J_c is a factor of 2–3 larger than we would expect for this film, probably attributable to the fact that the screening currents in reality decay rather more slowly in this thin film than the assumed exponential dependence. In practice the two fit parameters are strongly correlated and good agreement can be obtained with a fairly wide range of paired values. Fortunately the flux trapped in the antidot (integrated just above the film over a circle of radius $R+\lambda_{\mathrm{eff}}$) is rather insensitive to the specific choice, and corresponds to about 15 additional flux quanta

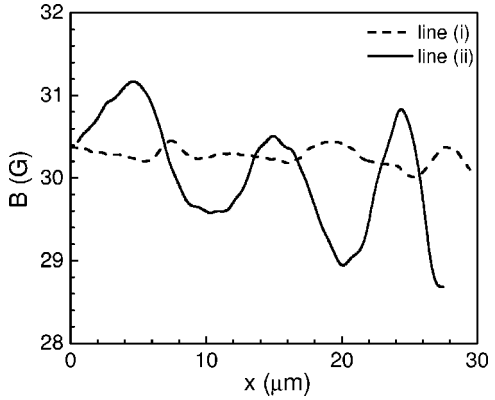

FIG. 8. Line scans along (i) the vortex channeling direction and (ii) perpendicular to it (but still along a chain of antidots) as indicated in Fig. 6(d).

trapped in each antidot, nearly an order of magnitude larger than the field-cooled saturation number estimated earlier. After reversal of the field sweep direction, the images (not shown) initially look almost identical to Fig. 6(c), with a very small gradual decrease in average magnetic induction. Upon reducing the field to 28 Oe (henceforth defined as H^*) [Fig. 6(d)], however, the flux suddenly starts flowing out of the holes towards the edge along the direction of maximum induction gradient. Surprisingly, at this point the fourfold image symmetry is lost in favor of an approximate twofold one, and almost unbroken flux stripes can be seen at and between the holes along the channeling direction. We name this phenomenon *flux streaming* to distinguish it from channeling, which largely preserves the fourfold symmetry. As the field is decreased further more vortices leave the sample and the holes increasingly become darker than the surrounding YBCO film [Figs. 6(e)–6(g)]. As the sense of the applied field is reversed, vortices of the opposite sign (black) appear to become, in turn, channeled along the antidots [Figs. 6(h) and 6(i)]. When the field sweep is reversed a second time, symmetry-breaking (black) flux "streaming" is again observed at the same absolute value of the field [Fig. 6(j)]. Reduction of the field to $H=0$ Oe [Fig. 6(l)] leads to a scan where the antidots appear white with respect to the interstitial film. Although this image looks superficially similar to Fig. 6(c) we now have black flux trapped in the film and empty holes, while on the first leg of the cycle the antidots were filled with white flux and the YBCO film was largely empty. A close inspection of the scans after the first field reversal also reveals some flux bundles trapped by particularly strong natural pinning centers in the film (smaller white spots between the holes). Figure 8 shows line scans across the image at $H=28$ Oe after the first field sweep reversal [Fig. 6(d)] along the direction of the arrows shown. This makes the broken symmetry particularly evident, with very weak induction modulation along the direction of vortex motion and deep modulation orthogonal to it.

The contrasting behaviors of the antidots and the interstitial YBCO film can be illustrated by making local magnetization ($M_l=B_l-H_a$) loops with the Hall sensor parked just above the sample at a desired location. Figure 9 shows two such loops captured after repeatedly cycling the applied field between −32 and 32 Oe, for the disk-shaped sample at 77 K. The solid points are taken with the Hall probe above an antidot and the open circles are captured at an interstitial position as indicated in the sketch. As expected, the remanent flux trapped in the antidots is considerably less than for the interstitial YBCO film. In addition the characteristic cusp where vortex streaming starts to occur after the reversal of field sweep direction is very clear. The image contrast of the antidots is presumably inverted where the two curves cross one another and occurs close to the field we define as H^* on the basis of the evolution of successive images.

In Fig. 10 we explore the influence of the maximum applied field (H_0) on the magnetization dynamics of the YBCO disk after ZFC to 77 K. In each case the applied field was increased to H_0 and then gradually reduced until the onset of flux exit out of the film close to H^* (in the direction of the arrows indicated). Figures 10(a)–10(d), 10(e)–10(h), and 10(i)–10(l) show the situations for maximum field excursions of 32, 28, and 6 Oe, respectively. In the first two rows we see that the onset of flux channeling (H^*) occurs after the field has been reduced to 24, and 20 Oe, respectively. For these scans (and other sets not shown), while H^* depends on the maximum applied field H_0, *their difference is approximately constant* $H_0-H^*\cong 8$ Oe. We note here that $H_0-H^*\cong 2\ H_p^{\mathrm{exp}}$, but further studies of this complex system are needed before we can say whether or not this is a significant observation. In contrast, for the third row when the applied field is only swept out to 6 Oe ($H_0<8$ Oe), we do not observe flux chan-

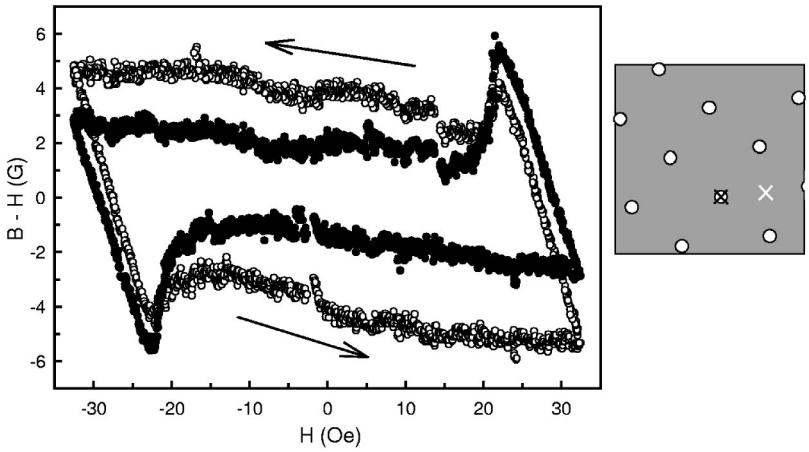

FIG. 9. Local magnetization loops measured at a point between antidots (white cross in sketch), open circles, and above an antidot (black cross in sketch), full circles.

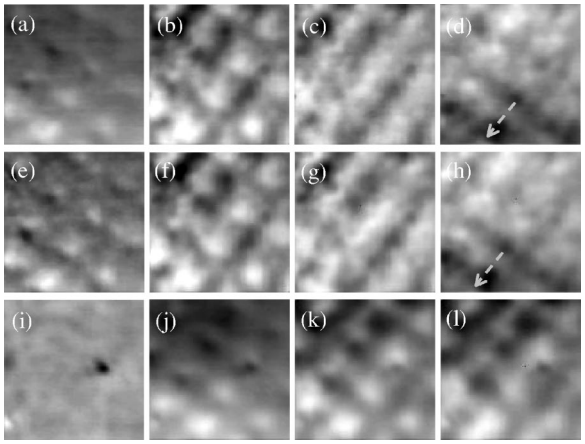

FIG. 10. SHPM scans on the YBCO disk ZFC to 77 K after subsequent field excursions to three different maximum fields (H_0): (a) $H=4$ Oe (GS$\sim$3.3 G), (b) $H=H_0=32$ Oe (GS$\sim$5.1 G), (c) $H=H^*=24$ Oe (GS$\sim$3.5 G), (d) $H=23$ Oe (GS$\sim$4.5 G); (e) $H=4$ Oe (GS$\sim$1.7 G), (f) $H=H_0=28$ Oe (GS$\sim$4.4 G), (g) $H=H^*=20$ Oe (GS$\sim$2.6 G), (h) $H=19$ Oe (GS$\sim$3.7 G); and (i) $H=0$ Oe (GS$\sim$1.1 G), (j) $H=4$ Oe (GS$\sim$2.1 G), (k) $H=H_0=6$ Oe (GS$\sim$2.4 G), (l) $H=0$ Oe (GS$\sim$2.0 G). H^* is the field at which vortex channeling is first observed.

neling out of the disk, even at $H=0$. Clearly the self-field due to the trapped flux is playing a key role in its magnetization dynamics. The same qualitative features are observed in scans on the square YBCO sample, although in this case we find $H_0-H^*\cong 4$ Oe at 77 K. This difference probably arises due to the fact that the scans were captured at different distances from the edge of the film in the two cases.

IV. DISCUSSION AND MODEL OF FLUX CHANNELING

In the following we discuss our results qualitatively in the light of a few well-established models, then present a simple classical electrodynamics model of flux channeling that appears to qualitatively reproduce many of our results. If we initially ignore the presence of the antidots we might expect the penetration field at the very edge of the sample to be limited by the geometrical barrier,[15] and given by $H_p \cong H_{c1}\sqrt{2d/W}$, where d, W are the thickness and width of the film, respectively. Using the estimate of $H_{c1}\sim 30$ Oe at 77 K, this yields a value of $H_p\sim 0.4$ Oe. It is not surprising that this is an order of magnitude smaller than the value we measure since our probe is situated relatively far from the edge of the sample in both cases. This can be accounted for if we approximate our samples as homogeneous superconducting disks, when it is known that the position from the center, r_p, of the penetrating flux front at an applied field H_p is given by[16]

$$r_p = a/\cosh(2H_p/J_c d), \tag{2}$$

where a is the disk radius, and J_c and d are the critical current density and thickness of the film. Assuming $J_c\cong 2\times 10^6$ A/cm^2, the two approximate locations, r_p, of our scans in the two samples (0.7 and 0.5 mm) would yield penetration fields of 22 and 32 Oe, respectively, almost an order of magnitude larger than the experimentally observed values. It is therefore evident that the presence of the antidot array strongly enhances flux penetration in our samples. Clearly our data can only be fully understood in terms of a model that includes the full topological complexity of our samples. We are not aware of any theoretical studies that have addressed flux penetration in antidot arrays in the limit $R\gg\lambda$, and would like to encourage work in this area.

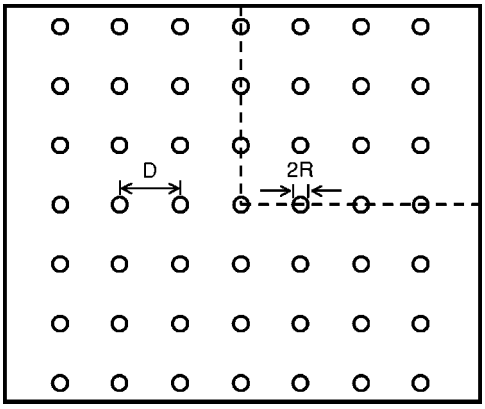

FIG. 11. Sketch of the model sample containing a square array of holes with aspect ratio $D/2R=4$ as for our samples. The upper right-hand side quadrant was discretized into a 50×60 point grid in the calculation.

For a more reasonable *qualitative* description of vortex channeling and other features observed in our ZFC scans, we consider a rectangular superconducting film with a square array of equidistant holes, as sketched in Fig. 11. The ratio between the hole diameter and their separation along one of the lattice vectors is the same as for our films (2.5:10). The two-dimensional problem of flux penetration into a thin superconducting film with an arbitrary shape can be solved numerically from first principles.[17] The main principle is to derive an integral equation for a quantity that is defined only inside the superconductor, and then integrate this equation as a function of time to obtain this quantity under different later conditions. Briefly, the two components of the sheet current $\mathbf{J}(x,y)=(J_x,J_y)$ may be expressed in terms of a scalar function $g(x,y)$, which represents a local magnetization: $J_x=\partial g/\partial y$ and $J_y=-\partial g/\partial x$. The perpendicular component of the field is given by

$$H_z(\vec{r}) = H_a + \int_A Q(\vec{r},\vec{r}')g(\vec{r}')d^2r', \tag{3}$$

with the integral kernel $Q(x,y;x',y')$ following from the Biot-Savart law. On a spatial grid $\mathbf{r}_i=(x_i,y_i)(i=1\ldots N)$ the integrand (1) may be expressed as a matrix multiplication,

$$H_z(\vec{r}_i) = H_a + \sum_j Q(\vec{r}_i,\vec{r}_j)g(\vec{r}_j), \tag{4}$$

while the scalar function is

$$g(\vec{r}_i) = \sum_j Q^{-1}(\vec{r}_i, \vec{r}_j)(H_z(\vec{r}_j) - H_a), \tag{5}$$

where the matrix Q^{-1} is obtained by inverting the matrix Q. As a last step, the equation of motion for $g(x,y,t)$ is obtained from the induction law and other material laws. All other desired quantities then follow from the Maxwell equations in the continuum theory, which was recently generalized to allow for an arbitrary London penetration depth.[18] The integral

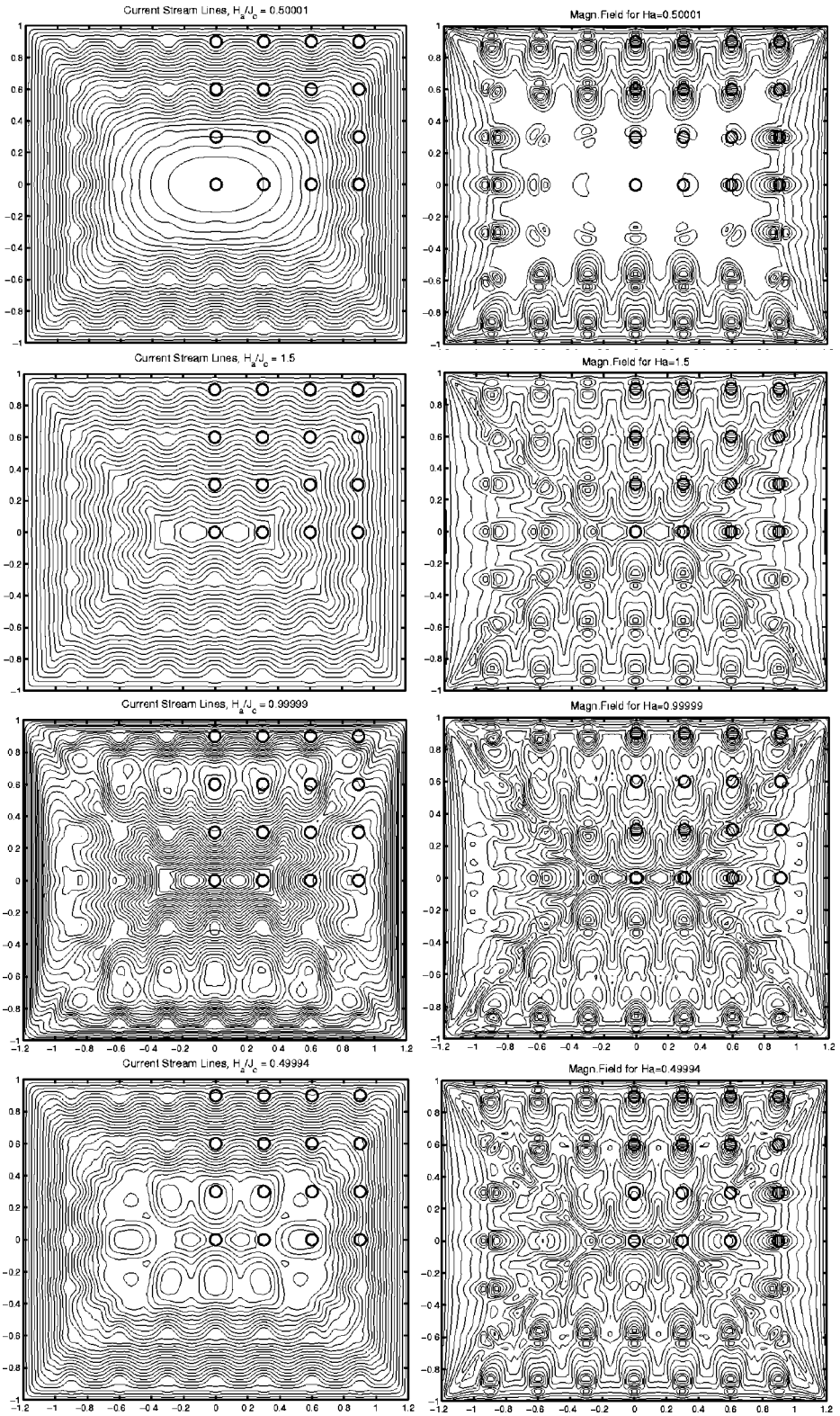

FIG. 12. Current streamlines (left), and contours of the magnetic field (right) for our model sample. The applied magnetic field increases and then decreases again from top to bottom $H_a/J_c = 0.5$, 1.5, 1, and 0.5.

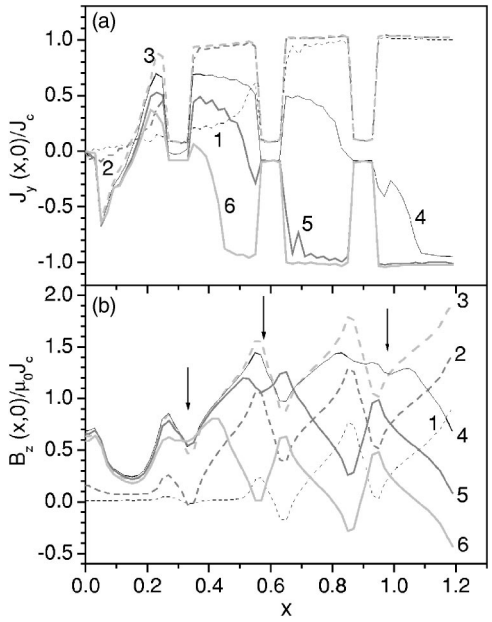

FIG. 13. Sheet current density (a) and magnetic induction (b) along the line $y=0$, for increasing applied fields of $H_a/J_c=0.5$, 1, and 1.5 (curves 1 to 3), and decreasing fields of $H_a/J_c=1$, 0.5, and 0 (curves 4 to 6). Arrows indicate (for decreasing fields) positions where the magnetic induction is flattened (curves 4 to 6), i.e. vortex streaming.

equation implicitly contains Maxwell's equations, the material equations, the boundary conditions, and the time-dependent applied field, which acts as the driving force. Details of the method, which uses matrix inversion on a spatial grid, can be found in Ref. 18.

For our problem, the top right-hand quadrant of our model sample was discretized with a 50×60 point spatial grid. The London penetration depth was taken to be 370 nm, and the constitutive law for the nonlinear resistivity was taken to be $\rho=\rho_0(J/J_c)^{n-1}$, with the resulting creep exponent being $n=20$. For the points on the grid inside the holes, a critical current density 10 times smaller than that in the film was used to describe the antidots. Numerical simulations were performed by sweeping the applied field up to a maximum of $H_a/J_c=1.5$ followed by a sweep reversal to $H_a/J_c=-0.5$, with a constant sweep rate magnitude. Some of the resulting current streamlines and magnetic field contours are shown in Fig. 12, for increasing fields of $H_a/J_c=0.5$, 1.5, and decreasing fields of 1 and 0.5. Line scans along $y=0$ yield the sheet current density $J_y(x,0)$ and the magnetic induction $B_z(x,0)$ along a line connecting the centers of holes. These are illustrated in Fig. 13 for $H_a/J_c=0.5$, 1, 1.5, 1, 0.5, and 0. A close inspection of the simulations in Fig. 13(b) appear to reveal qualitative agreement with several of our experimental results:

(i) Upon field sweep reversal, B_z, at and between the antidots, flattens over substantial distances [locations at different fields indicated by arrows in Fig. 11(b)] in a very similar way to our observations of symmetry-breaking flux streaming out of the sample in Figs. 6 and 10. This phenomenon now has a simple physical interpretation since, for a given value of decreasing field, the flat regions correspond to the positions where $J_y(x,0)$ crosses zero and abruptly changes sign (rapidly saturating to $+/-$ the critical current on either side of this point). When this front between forward and reverse bulk screening currents lies at an antidot, the circulating currents (due to the trapped flux in the hole) add on *both* sides of it. Hence flux trapped in the hole is driven in both directions along the antidot chain. This will favor the formation of linear flux structures and the circulating supercurrents will be suppressed in favor of current components parallel to the antidot chains. Consequently these structures should be relatively stable, even after the screening current interface has swept further into the sample.

(ii) At a given position, after flux streaming is observed, a further decrease in the field results in an inversion of contrast of the peak in B_z, at the antidots, exactly as we observe in our scans after channeling.

(iii) The model predicts magnetic induction dipolelike structures near the hole positions, due to the truncation of bulk screening currents at the edges of the antidots. These are related to the singularities in magnetic induction found at the edges of current-carrying 2D conductors, and were observed in the magneto-optical experiments of Ref. 12. In our case one would not expect to resolve this fine structure experimentally due to the small actual hole size combined with the relatively large distance between sample and Hall probe. The latter point, in particular, means that rather few Fourier components of the stray field due to the antidot lattice are retained in the image, and fine detail around the holes tends to be lost. Nevertheless the qualitative agreement between, for example, the line scans of Fig. 5(a) and line 6 in Fig. 13(b) is rather good.

(iv) In practice our model sample is only about seven holes wide, while the real sample is $\sim$200 holes wide. As a consequence the model greatly exaggerates the induction gradients at the holes, and one should not be surprised that flux penetration is dominated by the sample geometry, and effects due to the antidot lattice are weak. In Fig. 14 we compare induction contours of the penetration process in samples, which are identical except for the orientation of the antidot lattice at $H_a/J_c=1.5$. The left-hand side of Fig. 14 shows the situation discussed above where the unit vectors are parallel to the sample sides, whereas in the right-hand side of Fig. 14 the lattice vectors have been rotated 45° away from them. Careful examination of the induction profiles reveals a pronounced tendency for the contours to bow out along the lattice vectors of the 45° array (parallel to the black arrows) which is not mirrored in the other array. This appears to be a manifestation of channeling when the direction of maximum field gradient does not coincide with one of the lattice vectors of the antidot array. Vortex channeling can be attributed to at least three factors: (a) The mean screening current densities between the antidots are up to $\sim$33% larger than elsewhere, and vortices will consequently penetrate faster in these regions. (b) The local current distribution can be approximated by the superposition of the roughly uniform bulk screening currents and the loop currents circulating the antidots. These currents subtract on the sample edge side of the antidot and add on the sample center side. As a consequence the Lorentz force for additional penetration of flux trapped in the holes is enhanced. (c) The orientation of the

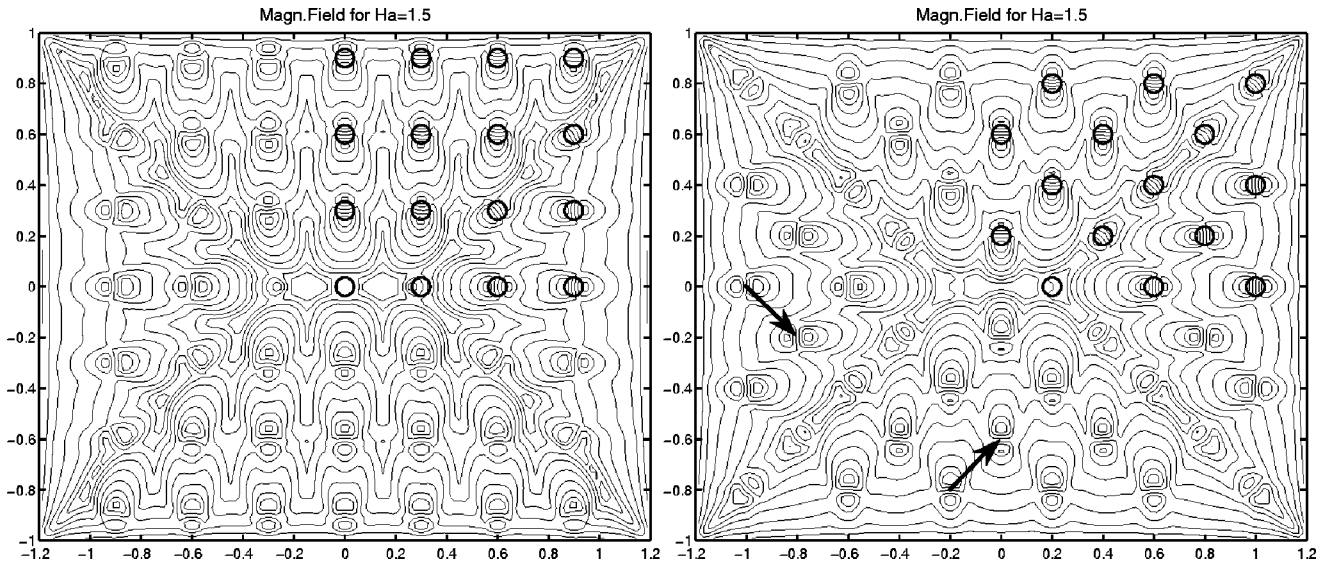

FIG. 14. Comparison of contours of magnetic induction after the applied field was increased from zero to $H_a/J_c=1.5$ for the sample sketched in Fig. 11 (left-hand side), and an otherwise identical sample with the lattice vectors of the array rotated by 45° (right-hand side).

array of holes imposes geometrical constraints on the direction of current flow around it, leading to a tendency for induction profiles to follow the antidot lattice vectors as in Fig. 14.

The simulations illustrated in Figs. 12–14 were performed for a finite penetration depth of 370 nm, but the results of the same model with $\lambda=0$ were almost identical to these. Hence, it appears that the flux channeling and streaming phenomena observed in these materials may be geometrical effects that depend primarily on the shape and topology of the sample. At the same time the saturation number of trapped flux quanta in the antidots in ZFC measurements is only 15. This is not a very large number and we are consequently unable to rule out that discrete vortex phenomena may also be playing an important role. The asymmetry that we have observed in flux entry and exit could form the basis of alternate vortex ratchet devices, and simulations of the type described here should provide a powerful tool for optimizing their properties.

V. CONCLUSIONS

SHPM scans performed on our samples after field cooling to 77 K in low applied fields have shown that a regular array of 2.5-μm-sized antidots with 10-μm separation in a YBCO thin film can trap all the flux lines in fields up to 0.4 Oe (approximately the earth's field), which could be important for noise reduction in unshielded HTS SQUIDs for cost-effective applications like magnetocardiography, airborne mineral exploration, or nondestructive testing with SQUID microscopy. ZFC scans revealed that the penetrating flux is channeled along chains of antidots in the direction of maximum magnetic induction gradient, which is a microscopic confirmation of the fourfold symmetry recently reported during flux penetration in similar samples. Upon field sweep reversal we observed flux lines streaming out of the holes towards the edge along the direction of maximum induction gradient and almost unbroken flux stripes can be seen at and between the holes along the channeling direction. We estimate that the antidots can preferentially trap about 15 flux quanta in these ZFC experiments. Many features of the observed flux dynamics appear to be well-described qualitatively by a classical electrodynamics model indicating that the observed phenomena may be geometrical effects depending primarily on the shape and topology of the sample. Both our experimental results and numerical simulations promise to be of considerable importance for applications of patterned thin-film structures, e.g., vortex ratchet-based rectifiers, pumps, collective step motors, and lenses.

ACKNOWLEDGMENTS

This work was supported by EPSRC Grant No. GR/R46489/01, by the Ministry of Education and Research under the CERES program in Romania, and the ESF VORTEX network.

[1] J. F. Wambaugh, C. Reichhardt, C. J. Olson, F. Marchesoni, and F. Nori, Phys. Rev. Lett. **83**, 5106 (1999).

[2] J. E. Villegas, S. Savel'ev, F. Nori, E. M. Gonzales, J. V. Anguita, R. Garcia, and J. L. Vincent, Science **18**, 1188 (2003).

[3] R. Wördenweber and P. Dymashevski, Physica C **404**, 421 (2004); R. Wördenweber, P. Dymashevski, and V. R. Misko, Phys. Rev. B **69**, 184504 (2004).

[4] H. Weinstock, Physica C **209**, 269 (1993).

[5] B. Y. Zhu, F. Marchesoni, V. V. Moshchalkov, and F. Nori, Phys. Rev. B **68**, 014514 (2003).
[6] L. Civale, A. D. Marwick, T. K. Worthington, M. A. Kirk, J. R. Thompson, L. Krusin-Elbaum, Y. Sun, J. R. Clem, and F. Holtzberg, Phys. Rev. Lett. **67**, 648 (1991).
[7] A. Crisan, S. Fujiwara, J. C. Nie, A. Sundaresan, and H. Ihara, Appl. Phys. Lett. **79**, 4547 (2001); A. Crisan, P. Badica, S. Fujiwara, J. C. Nie, A. Sundaresan, Y. Tanaka, and H. Ihara, *ibid.* **80**, 3566 (2002).
[8] M. Baert, V. V. Metlushko, R. Jonckheere, V. V. Moshchalkov, and Y. Bruynseraede, Phys. Rev. Lett. **74**, 3269 (1995); A. Castellanos, R. Wördenweber, G. Ockenfuss, and A. v.d. Hart, Appl. Phys. Lett. **71**, 962 (1997).
[9] R. Wördenweber, P. Lahl, and P. Selders, J. Low Temp. Phys. **130**, 435 (2003).
[10] M. Pannetier, R. J. Wijngaarden, I. Fløan, J. Rector, B. Dam, R. Griessen, P. Lahl, R. Wördenweber, and P. Lahl, Phys. Rev. B **67**, 212501 (2003).
[11] A. Oral, S. J. Bending, and M. Henini, Appl. Phys. Lett. **69**, 1324 (1996).
[12] J. Eisenmenger, P. Leiderer, M. Wallenhorst, and H. Dötsch, Phys. Rev. B **64**, 104503 (2001).
[13] A. Crisan, A. Pross, R. G. Humphreys, and S. Bending, Supercond. Sci. Technol. **16**, 695 (2003).
[14] J. Pearl, Appl. Phys. Lett. **5**, 65 (1964).
[15] E. Zeldov, A. I. Larkin, V. B. Geshkenbein, M. Konczykowski, D. Majer, B. Khaykovich, V. M. Vinokur, and H. Shtrikman, Phys. Rev. Lett. **73**, 1428 (1994).
[16] E. H. Brandt, M. V. Indenbohm, and A. Forkl, Europhys. Lett. **22**, 735 (1993).
[17] E. H. Brandt, Phys. Rev. B **52**, 15 442 (1995).
[18] E. H. Brandt, Phys. Rev. B **64**, 024505 (2001).